Photovoltaic power forecast based on satellite images considering effects of solar position

Zhiyuan Si, Ming Yang [*], Yixiao Yu, Tingting Ding

Key Laboratory of Power System Intelligent Dispatch and Control, Shandong University, Jinan 250061, China

HIGHLIGHTS

- A satellite image-based photovoltaic power forecasting model is proposed.
- A nonlinear cloud movement forecasting method based on deep learning is proposed.
- An algorithm for intra-hour cloud condition estimation is established.
- An algorithm for recognizing the cloud region that blocks sunlight is designed.

ARTICLE INFO

ABSTRACT

The rapid variation of clouds is the main factor that causes the fluctuation of photovoltaic power.[1] The satellite images contain plenty of information about clouds, applicable for photovoltaic power forecast. However, in practice, two main factors obstruct the application of the satellite images: 1) the relatively low update frequency of the satellite images mismatches the photovoltaic power forecasting frequency, and 2) the cloud region that blocks the sunlight changes significantly with time. In this paper, a novel satellite image-based approach for photovoltaic power forecast is proposed to overcome these obstacles and achieve accurate forecasting results. Firstly, concerning the hourly updated satellite images, a nonlinear cloud movement forecasting model, considering the thickness and shape changes of the cloud, is presented to forecast the hourly variation of the images. Secondly, an active cloud region selection rule is derived based on the changing solar position to dynamically select the cloud region that blocks the concerned photovoltaic power station in a satellite image. Thirdly, a sequential cloud region selection algorithm is provided to estimate the intra-hour variation of the cloud to match the photovoltaic power forecasting frequency. Finally, the photovoltaic power is predicted using the XGBoost algorithm concerning the effects of the cloud and other influencing factors. Testing results show that the proposed method can achieve more accurate photovoltaic power forecasts using the low update frequency satellite images. Meanwhile, the superior performance compared with other benchmarks also verifies the effectiveness of considering cloud information obtained by the proposed method for photovoltaic power forecast.

1. Introduction

With the rapid growth of the world economy, fossil energy utilization and climate change are becoming critical global issues [1]. Developing renewable energy has become one of the solutions to overcome those issues. Being clean, safe, and inexhaustible, solar energy has been widely applied worldwide [2]. Exemplified by the data in 2019, the newly installed photovoltaic (PV) capacity exceeded 97GW globally, showing a continuously rising trend and broad application perspectives. However,

the randomness and fluctuation of PV power hinder its utilization efficiency and bring the challenges to system stability [3], frequency response [4], load prediction [5]. To alleviate the impact of the uncertainty of the PV power output, accurate PV power forecast has become an indispensable module in energy management and cost reduction. The accurate prediction of PV power has great significance for improving system reliability [6], saving fuel costs the ancillary costs [7], and making strategies in the electricity market for load aggregators [8].

Traditional solar forecasting methods usually adopt the numerical weather prediction (NWP) model to predict PV power. Based on a series

Nomenclature

Acronyms

PV	Photovoltaic
ACRS	Active cloud region selection rule
SCRS	Sequential cloud region selection algorithm
XGBoost	Extreme Gradient Boosting
NWP	Numerical weather prediction
TSIs	The ground-based total sky imagers
CNN	Convolutional neural network
LSTM	Long short term memory network
ANN	Artificial neural network
PIV	Particle image velocimetry
Conv-LSTM	Convolutional long short term memory network
CART	Classification and regression trees
Conv3D	Three-dimension convolutional layer
MSE	Mean squared error
SSIM	Structural similarity index measurement
NMAE	Normalized mean absolute error
NRMSE	Normalized root mean square error

CORR	Correlation coefficient
PM	Persistence method

Parameters

T	Time index
α_s	Solar zenith angle
φ	Latitude
ω	Time angle
δ	Declination angle
γ_s	Solar azimuth angle
R^2	Coefficient of determination

Functions

$\sigma(\bullet)$	Sigmoid activation function
$tanh(\bullet)$	Hyperbolic tangent function
$Obj(\bullet)$	Objective function
$Arccos(\bullet)$	Arc cosine function
$Cov(\bullet)$	Covariance
$Var(\bullet)$	Variance

of differential equations, NWP model generates the future weather conditions, which can be fed to the forecasting model to achieve PV power forecast. In [9], a machine learning technique is developed to obtain the PV power forecast by using irradiance, temperature, humidity, and wind direction. Similarly, three different NWP models [10], i.e., the North American mesoscale forecasting system, the global forecasting system, and the short-range ensemble forecast, are selected to predict PV power, both on the regional level and single-site level. Since the NWP models have a coarse spatial and temporal resolution, there is a consensus that PV power forecasting methods based on the NWP model are more suitable for short and long-term forecasts [11].

For the ultra-short-term PV power forecast, the movement and dissipation of clouds are crucial factors that affect PV power. Given cloud images can reflect cloud shape, transparency and distribution, plenty of forecasting methods are proposed based on cloud images. The literature can be briefly classified into two categories.

The first kind of method bases on the observation of the ground-based total sky imagers (TSIs), which can provide sky images with high spatial and temporal resolution (about 1 min [12,13] or even 30 s [14]). Initially, TSIs were utilized for cloud detection [15], cloud classification [16], and cloud recognition [17]. Since TSIs could offer the cloud conditions with an excellent temporal resolution, TSIs-based PV power forecasting methods have attracted attention in recent years. In [18], a 3D cloud detection and tracking system for irradiance forecast using multiple TSIs is proposed, which can track clouds under various cloud conditions. In [19,20], the convolutional neural network (CNN) is employed to establish a mapping model between the TSI images and irradiance. In [21], the real-time mapping relationship between the TSI images and irradiance is established by combining long short term memory (LSTM), CNN, and artificial neural network (ANN). Meanwhile, TSI images have been utilized for solar ramp event forecast, which shows a robust performance [22]. However, since the monitoring scope of TSI is limited, the effective forecasting horizon of this kind of method is typically less than 2 h [23]. Meanwhile, the high installation and maintenance cost keeps TSIs from being widely used.

The second kind of method uses satellite images as inputs. Although the satellite images-based methods are qualitatively similar to the TSIs-based PV power forecasting methods, there are a few significant differences between them. The satellite image includes visible [24] and infrared images [25], which are both taken from satellite-based sensors flying overhead. Satellite visible images reflect the reflection of sunlight from the ground and clouds, and are widely used in monitoring changes

in clouds. Satellite infrared images can reflect the temperature on the earth surface, making them suitable for weather forecast. Compared with TSIs, the satellite images can capture a much more extensive sky range and can be reliably obtained from various meteorological organizations. Therefore, the satellite image provides an alternative of TSI for PV power forecast, especially for the relatively long time scales, e.g., 2–4 h. Satellite images have been utilized in irradiance quantification [26], and irradiance forecast [27,28]. Several mapping models between the satellite images and solar irradiance have been developed recently. In [29], Hammer translated the satellite images into the cloud index and used it to predict the irradiance. In [30], Marquez extracted the cloud features from satellite images and predicted global horizontal irradiance by combining the cloud indexes of the selected regions with the ANN. In [31], an hour ahead forecasting method of the spatial average irradiance is proposed using the NWP and satellite images. Although satellite images play a significant role in irradiance prediction, obstacles still exist when the satellite images are directly applied to the ultra-short-term PV power forecast.

The uncertainty of forecasting cloud motion causes the first obstacle. The first step of the image-based PV power forecast is to estimate the cloud motion to obtain the forecasting cloud images. Then the occlusion of the sunlight by clouds can be inferred. Therefore, an accurate forecast of cloud motion has significance for the PV power forecasting tasks. In preceding studies, several image feature matching methods, e.g., the cross-correlation method [32], the particle image velocimetry (PIV) method [33], and the optical flow method [34,35], have been proposed to predict the cloud movement. To simplify the model, these methods usually treat clouds as rigid bodies and assume that they move in a straight line with a cloud motion vector. However, the thickness and shape of clouds dynamically change over time, and it would be rough to use a linear formula to describe the future variation of the cloud cluster. More recently, the convolutional long short term memory algorithm (Conv-LSTM) [36] is designed to predict future rainfall radar images by using a series of historical images. Such study inspires us to utilize the Conv-LSTM model for cloud motion forecast, considering the cloud nonlinear movement trajectories.

The second obstacle is cloud region identification. The PV power station can be represented by a one-pixel point in the satellite image. Recent researches directly utilize this pixel [30] or the region centered on this pixel [31] to reflect the cloud shielding effect against the sunlight. Differ from the TSI-image, the satellite images contain no information about the sun. It is hard to directly recognize which cloud region

blocks the sunlight in the satellite images. Meanwhile, since the sun constantly moves in a day, the solar zenith angle and azimuth angle change with time significantly. Therefore, dynamically recognizing the cloud region that blocks the sunlight in satellite images is another crucial problem. More recently, sun positioning methods are proposed for finding the solar facula [37] and determining the solar position [38]. Such study inspires us to accurately locate the cloud region that blocks the sunlight in the satellite images through some physical derivation and formula calculation.

The third obstacle is the relatively low update frequency of the satellite images. Nowadays, the common temporal resolution of publicly accessible satellite images is one hour [39,40], which cannot match the general temporal resolution requirements of the ultra-short-term PV power forecast, e.g., 15 min for most power grids worldwide. This obstacle also limits the application of satellite images on PV power forecast.

In this paper, a novel satellite image-based approach for PV power forecast is proposed to address the obstacles mentioned above by using the low update frequency satellite images. The proposed method aims to achieve a better forecasting performance by considering cloud information obtained by the active cloud region selection rule (ACRS) and the sequential cloud region selection algorithm (SCRS). The XGBoost [41] model has been widely used in power prediction, showing its efficiency and effectiveness. Therefore, the XGBoost model is utilized in this paper to establish the mapping relationship between the input variables and output variables, achieving an accurate PV power forecast. The main contributions of this paper are as follows.

1) The Conv-LSTM is applied on the hourly satellite image forecast, which takes the nonlinear cloud motion into account, providing more accurate cloud movement trajectories. Meanwhile, the thickness and shape changes of the cloud are also considered in the model.
2) The ACRS rule is derived considering the solar position and the PV station location, which can accurately locate the cloud region that blocks the concerned PV power station in the satellite images. By this means, the extracted cloud features are more relevant to the PV power changes and bring more accurate forecasting results.
3) The SCRS algorithm is developed according to the ACRS rule. It can predict the cloud condition at any given time step, i.e., 15 min, from the low update frequency satellite images. Thus, the temporal resolution requirement of ultra-short-term PV power forecast can be satisfied.

The rest of this paper is organized as follows. Section II introduces the principles of Conv-LSTM and XGBoost. Section III presents the main methods proposed in this paper, i.e., the hourly image forecasting method, the ACRS rule and the SCRS algorithm. Section IV introduces the simulation process and results. Finally, the conclusions are drawn in Section V.

2. Methodology

In the proposed approach, Conv-LSTM is utilized to predict the cloud movement and XGBoost is adopted to establish the PV power forecasting model. This section briefly introduces the principles of these algorithms.

A. Conv-LSTM networks

Conv-LSTM combines the advantages of CNN [42] and LSTM [43], which is good at mining temporal features and describing local spatial characteristics of images [36,44]. The structure of the Conv-LSTM unit is shown in Fig. 1, which roughly includes four parts, i.e., the convolution layer, an input gate, a forget gate and an output gate.

The convolution layer is applied to extract the spatial features contained in the satellite images. The forget gate is used to determine which part of the old information needs to be dropped. The input gate is used to
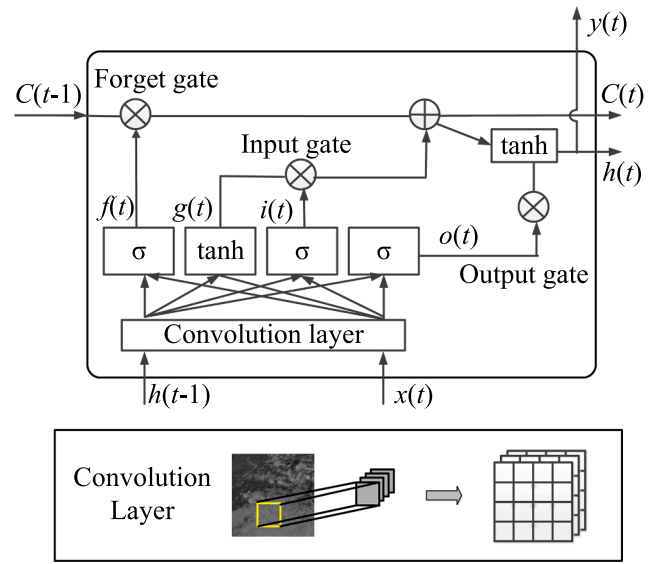

Fig. 1. The structure of Conv-LSTM units.

update the new memories with newly coming data. And the output gate produces the output of the Conv-LSTM unit.

As illustrated in Fig. 1, the input x_t is fused with the output of the previous time step h_{t-1} to construct the input vectors of the model, and the vectors are input into the convolution layer. Secondly, the convolution filters are applied to extract features from the input to form the feature maps. The feature maps are pairwise to combine old and new information according to the corresponding rule shown in Eqs. (1)–(4). Then i_t, g_t, f_t and o_t can be obtained, where i_t and g_t represents the new memories that need to be updated, f_t represents the extent to which the old information should be forgotten, and o_t determines which part of the cell state will be exported. Finally, the new cell state C_t is activated through the hyperbolic tangent operation and multiplied by o_t to determine the output h_t. The working process [36] of the Conv-LSTM unit can be expressed as

$$i_t = \sigma(W_{xi} * x_t + W_{hi} * h_{t-1} + b_i), \tag{1}$$

$$g_t = tanh(W_{xc} * x_t + W_{hc} * h_{t-1} + b_c), \tag{2}$$

$$f_t = \sigma(W_{xf} * x_t + W_{hf} * h_{t-1} + b_f), \tag{3}$$

$$o_t = \sigma(W_{xo} * x_t + W_{ho} * h_{t-1} + b_o), \tag{4}$$

$$C_t = f_t {}^{\circ} C_{t-1} + i_t {}^{\circ} g_t, \tag{5}$$

$$h_t = o_t {}^{\circ} tanh(C_t), \tag{6}$$

where σ stands for the activation function, W represents the weight of each threshold layer, x_t represents the input image of time step t, b represents the bias corresponding to the gate, "$*$" denotes convolution operation, and "$\circ$" denotes the Hadamard product.

B. XGBoost

XGBoost is a boosting ensemble learning algorithm, which has been widely used in machine learning competitions in recent years. It can generate new trees iteratively by fitting the residual errors, forming a classifier with higher accuracy and stronger generalization ability [45,46]. XGBoost includes various classification and regression trees (CART), and its model can be expressed as

$$\widehat{y}_i = \sum_{k=1}^{K} f_k(x_i), f_k \in F, \tag{7}$$

where K is the number of the trees, F is a set of all possible CART trees, and f_k is a CART tree in F.

Optimizing the objective function is the key point of XGBoost. To learn the set of trees used in the model, the regularization goals are minimized as

$$Obj^{(t)} = \sum_{i=1}^{n} l(y_i, \widehat{y}_i^{(t-1)} + f_t(x_i)) + \Omega(f_t) + c, \tag{8}$$

where $\widehat{y}_i^{(t-1)}$ denotes the previous t-1 round prediction, y_i denotes the actual value, and $f_t(x)$ is a new CART tree at the t round. l represents the differentiable convex loss functions, $\Omega(f_t)$ represents the regularization item, and c represents a constant.

The generalization ability of the tree becomes stronger when the function value is smaller. To simplify the objective function, the Taylor second-order expansion is performed on the objective function. By removing all constant terms and rewriting the function, the objective can be approximately expressed as

$$Obj^{(t)} \approx \sum_{j=1}^{T} \left[w_j \sum_{i \in I_j} g_i + \frac{1}{2} \left(\sum_{i \in I_j} h_i + \lambda \right) w_j^2 \right] + \gamma V, \tag{9}$$

where V is the number of the leaf nodes, w_j is the score value of the j-th leaf node, I_j represents the sample on the j-th leaf node, g_i denotes the first derivative of the loss function l, and h_i denotes the second derivative of the loss function l.

Then, by taking the partial derivative, the optimal solution w_j^* of the optimization problem (9) can be expressed as

$$w_j^* = -\frac{G_j}{H_j + \lambda}, \tag{10}$$

where G_j represents the sum of all the g_i on the j-th leaf node, H_j represents the sum of all the h_i on the j-th leaf node, and λ is the regularization parameter.

And the optimal objective value $Obj^{'}$ can be obtained by bringing (10) into (9), as

$$Obj^{'} = -\frac{1}{2} \sum_{j=1}^{V} \frac{G_j^2}{H_j + \lambda} + \gamma V, \tag{11}$$

where γ is the regularization parameter. During the training process, XGBoost keeps constructing the error CART trees to improve the current model continuously, until getting satisfied forecasting performance.

3. Proposed forecasting approach

A. Overall Framework of the Approach

Fig. 2 provides the overall framework of the approach, including the data processing part, feature extraction part, and modeling part.

In the data processing part, the raw images are preprocessed to remove the diurnal effects using the satellite image standardized method, which can be found in our previous paper [47]. Then the hourly changes of the satellite images for the next several hours are estimated using the proposed cloud movement forecasting method based on the Conv-LSTM model. In the feature extraction part, the concerned cloud region in the satellite image is dynamically selected through a newly developed ACRS rule. Accordingly, the SCRS algorithm is presented to estimate the intra-hour variation of the cloud. Based on the ACRS and SCRS, the cloud features can be extracted at any time step from the hourly updated satellite images. In the modeling part, the PV power is predicted using the trained XGBoost model, concerning the estimated cloud conditions and other influencing factors. This section emphatically introduces the cloud movement forecasting method, the ACRS rule, the SCRS algorithm and the modeling process.
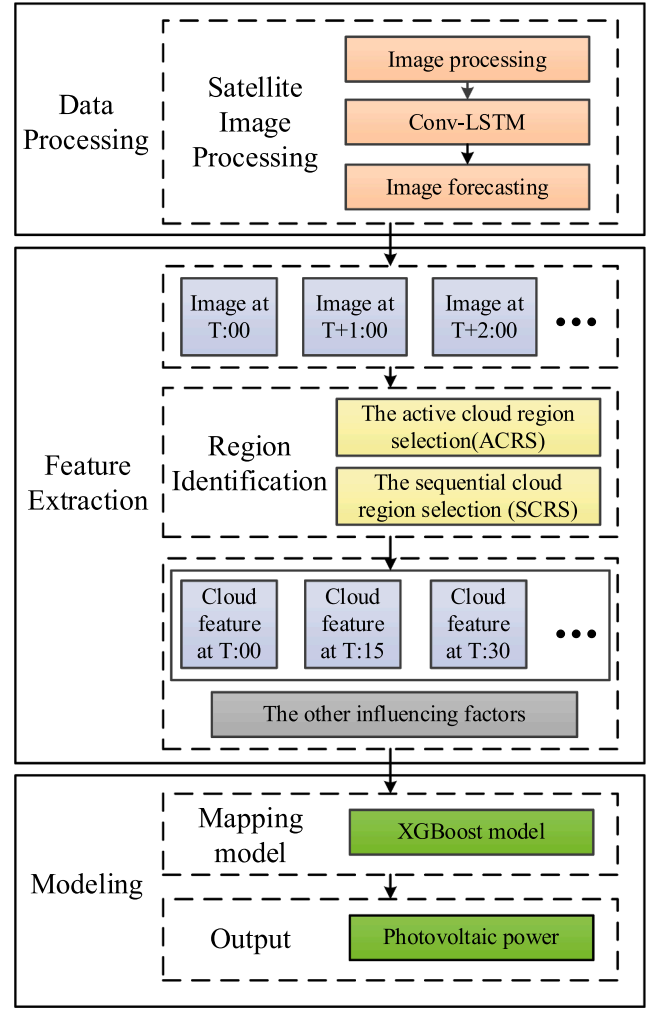

Fig. 2. The overall framework of the proposed approach.

B. Cloud Movement Forecasting Method

The satellite images contain plenty of information about the shape, transparency and movement trend of clouds. Predicting the changes of clouds among sequential satellite images is essential for the intraday PV power forecast.

In fact, the prediction of cloud movement is a nonlinear spatiotemporal sequence problem including time and space factors. Here, the time factor refers to the changes among continuous satellite images, and the space factor represents the spatial information of cloud movement contained in a satellite image. Since the Conv-LSTM is particularly suitable to deal with nonlinear spatiotemporal sequence problems, it is adopted to predict the satellite images and provide a more accurate nonlinear trajectory of cloud movement.

Fig. 3 shows the flowchart of the proposed cloud movement forecasting method. Suppose current time is T, and the historical satellite images at time T-2, T-1, and T are input into the Conv-LSTM model to predict the satellite images at time $T+1$, $T+2$, and $T+3$. Since the raw satellite image contains much cloud information of other regions, only a partial satellite image is selected and input into Conv-LSTM to predict the future cloud conditions. In this paper, the partial satellite image is set as a rectangular area centered on the location of the PV station, and the pixel size is 60×60. As illustrated in Fig. 3, in the approach, several Conv-LSTM layers are cascade connected to extract the satellite image features and one Conv3D layer is applied to convert 3D feature vectors into 2D images.
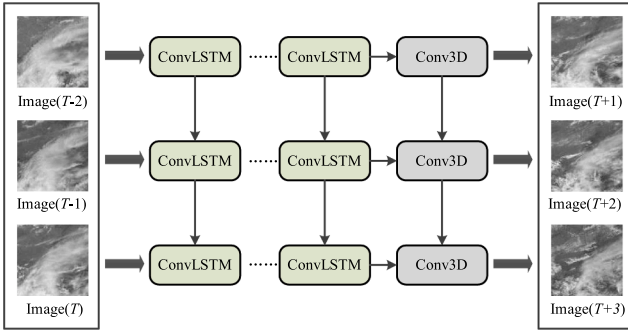
Fig. 3. The flowchart of the cloud movement forecasting method.

Firstly, the sequential satellite images are input into the convolution layers to extract the spatial information at successive moments, which consists of the feature vectors that represent the cloud distribution and thickness. Since the satellite image prediction task requires relatively fewer features, only four filters are constructed in the convolution layer. And the filter size is set as 3 × 3 to capture the cloud edge details. Secondly, LSTM is utilized to extract the temporal correlation characteristics contained in the spatial information at successive moments. According to the receptive field of the convolution filters, the satellite image can be divided into several small blocks, as illustrated in Fig. 1. Based on the LSTM, each block will obtain a temporal feature that reflects local changes in cloud shape and thickness. The changes of the clouds in the whole region are composed of the changes of each cloud block. It worth mentioning that the nonlinear motion of the cloud is fully considered in this method, since the temporal characteristics of each block are different, and this is quite different from current rigid body cloud movement estimation methods. Considering the complexity of the satellite image information and computational efficiency, 6 Conv-LSTM layers are selected in the proposed model.

Since multiple convolution filters are selected, the feature maps gained from each Conv-LSTM unit are three-dimensional. The three dimensions are image length, image width and channel number, respectively. And the Conv3D layer is applied to merge the channels to realize the conversion of 3D features to 2D images. Therefore, the predicted images can be obtained from the Conv3D layer.

Meanwhile, two loss functions, i.e., mean squared error (MSE) and the structural similarity index measurement (SSIM) are tested in this paper. According to the experimental results, the SSIM is selected as the loss function. The experimental results show that the nonlinear cloud movement trend and cloud shape can be better predicted by the Conv-LSTM model, mainly because it can establish the temporal relationship between the image sequences and consider the spatial changes of cloud clusters.

C. Active Cloud Region Selection

The brightness and darkness of the satellite visible images depend on the albedo of the object. The thick cloud owns high albedo and the corresponding cloud region in the satellite visible images shows a brighter hue. In contrast, the thin cloud region in satellite images shows a dark hue. Meanwhile, the brightness and darkness of the satellite visible image can be quantified by the pixel value, so the thickness of the cloud can be reflected by the pixel value. Since the spatial resolution of publicly accessible satellite images is about several thousand meters, the PV station can be represented as a pixel point in satellite images. In satellite images, the pixel value at the location of the PV station can reflect the cloud thickness vertically above the station. Most existing studies utilize this pixel to reflect the cloud shielding effect against the sunlight. However, sunlight rarely reaches the ground vertically, as illustrated in Fig. 4.

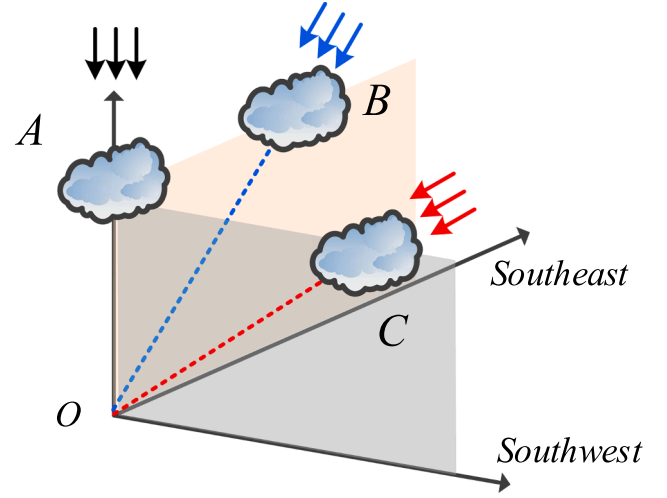Fig. 4 shows the schematic of the cloud blocking effect. Assuming a

Fig. 4. The schematic of the cloud blocking the sunlight.

PV station is located in the middle latitude of the northern hemisphere, obviously, almost all sunlight will come from the south. For PV station O, the sunlight in the morning comes from the southeast, which means that area B will block the sunlight. In the afternoon, the sunlight comes from the southwest, and the shielding effect of cloud area C should be concerned. It can be seen from Fig. 4 that the cloud region blocks the sunlight reaching the concerned PV station changes constantly, and it is not reasonable to always use area A, i.e., the vertical cloud area above the station, to reflect the cloud blocking effect. Therefore, accurate recognition of the cloud region that blocks the sunlight from reaching the PV power station is valuable for improving forecasting performance. Some recent studies [38] have used the solar position and related formulas to locate the facula in the ground-based images. These researches inspire us to recognize the concerned cloud region in the satellite images through a similar theory.

To address the obstacle of existing methods, the ACRS rule is derived to dynamically recognize the concerned cloud region. The key is to locate the intersection between the sunlight and the cloud in a satellite image, as illustrated in Fig. 5.

In the satellite image $I(x, y)$, assume that the PV station $O(x_0, y_0)$ is on the center of the image, the intersection between the sunlight and the cloud is S', and $S(x_s, y_s)$ represents the projection of point S' in the satellite image. In Fig. 5, α_s represents the solar zenith angle, γ_s represents the solar azimuth angle, H denotes the height of the cloud cluster, and L
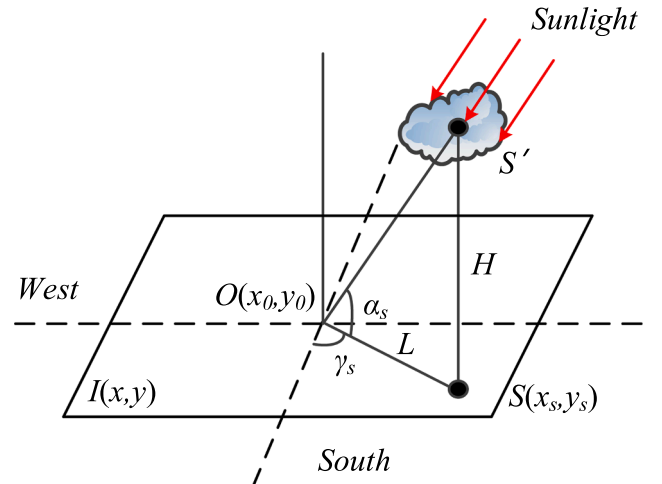

Fig. 5. The location of the intersection between the sunlight and the cloud in the satellite image.

denotes the distance between S and O. For a specific PV station, the solar zenith angle and the solar azimuth angle can be inferred by the related physical laws. Then, the angle of the PV station and sunlight can be determined. Ultimately, the cloud that intersects the trajectory of the sunlight is considered to be the concerned cloud region, which produces a shielding effect.

First, the solar zenith angle [37] can be calculated by

$$\alpha_s = arccos(sin\varphi sin\delta + cos\varphi cos\delta cos\omega), \tag{12}$$

where φ denotes the latitude, ω denotes the time angle, and δ denotes the declination angle. In Eq. (12), the time angle and the solar declination angle [37] can be respectively obtained by

$$\omega = (t - 12) \times 15^{\circ}, \tag{13}$$

$$\delta = 23.45^{\circ} sin(2\pi \times \frac{284 + d}{365}), \tag{14}$$

where d denotes the serial number of one day in a year.

Based on the solar zenith angle, the solar azimuth angle [38] can be calculated by

$$\gamma_s = arccos[(sin\alpha_s \times sin\varphi - sin\delta)/(cos\alpha_s \times cos\varphi). \tag{15}$$

According to the trigonometric relationships, L can be obtained from H, as

$$L = H/tan\alpha_s. \tag{16}$$

Finally, based on the L and γ_s, the intersection between the sunlight and cloud in the satellite images can be calculated as

$$x_s = x_o + L \times sin\gamma_s, \tag{17}$$

$$y_s = y_o + L \times cos\gamma_s. \tag{18}$$

where x_s and y_s represent the east–west and north–south distances from the intersection point S to O in the satellite image, respectively. And thus, the intersection $S(x_s, y_s)$ can be located in the satellite image.

It should be noted that the height of clouds may change with time more or less. But to simplify the calculation, the cloud height H is set as a constant empirically when formulating Eqs. (12)–(18). Therefore, to consider the estimation error of S caused by the assumption on H, instead of using point S solely, an area centered on the intersection point S, as the blue area R shown in Fig. 6, is selected to reflect the shielding effects of the clouds. And the size of the concerned cloud region is set to
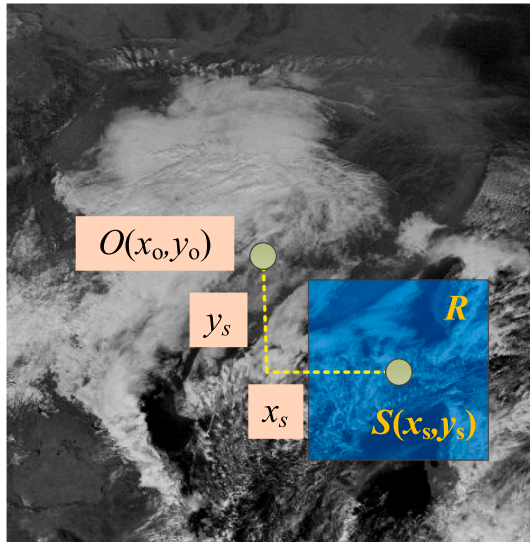
10×10 pixels.

D. Sequential Cloud Region Selection

The ACRS rule can locate the concerned cloud region that blocks the sunlight in the satellite image at any time. By implementing the ACRS rule on the satellite image simultaneously, the concerned cloud region can be recognized, and then the cloud features at the corresponding time can be extracted. However, the time resolution of publicly accessible satellite images is generally one hour, which makes it impossible to predict the intra-hour variation of PV power based on the low update frequency satellite images. Therefore, estimating the intra-hour satellite images through the low update frequency satellite images plays an indispensable role in PV power forecast. To match the general temporal resolution requirements of the ultra-short-term PV power forecast, the SCRS algorithm is developed based on the ACRS rule. The SCRS algorithm aims to estimate the intra-hour variation of the clouds and locate the concerned cloud region, which can also be divided into two steps. The first step is to predict the cloud condition at the given time step, e.g., 15 min in this paper, with respect to the low update frequency satellite images. And the second step is to use the ACRS rule to locate the concerned cloud region according to the predicted intra-hour cloud condition.

Clouds move slowly and continuously, making the cloud clusters have no significant changes in a short time. Based on this condition, three simple schemes for the intra-hour cloud conditions predictions are presented. To simplify the description, time is represented in the format
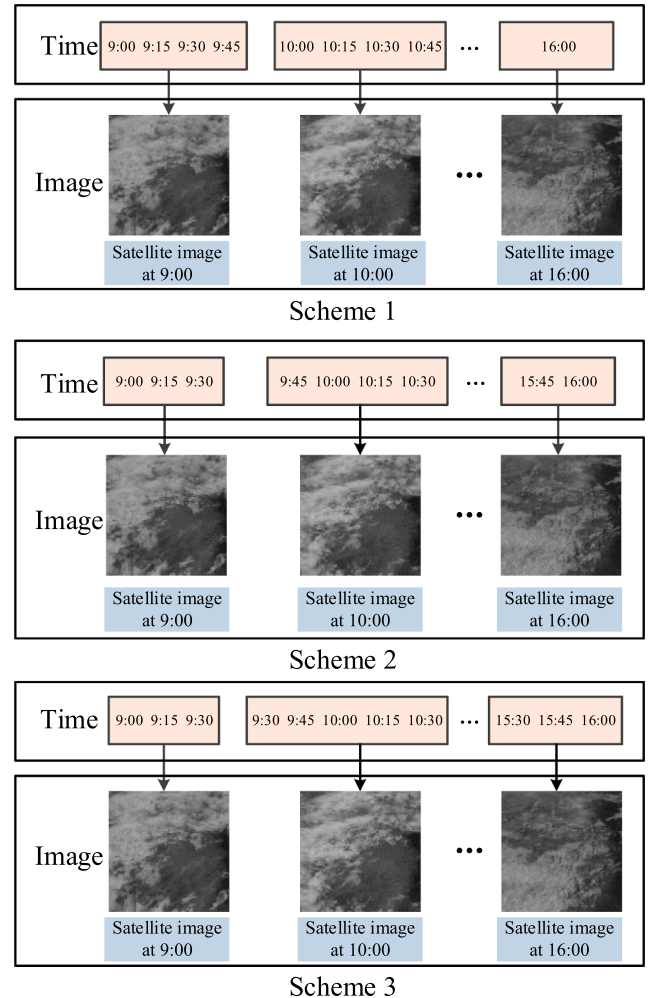

Fig. 6. The location of the concerned cloud region in satellite images.

Fig. 7. The principle of each SCRS scheme.

of *h:m*. Fig. 7 shows the principle of each SCRS scheme.

Scheme 1: When *m* = 0, 15, 30, or 45, the satellite image at *h:m* is represented by the satellite image at *h:00*. In another word, the satellite images at *h:m* are all represented by the satellite image at *h:00*.

Scheme 2: If *m* = 0, 15, or 30, the satellite image at *h: m* is represented by the satellite image at *h: 00*. And if *m* = 45, the satellite image at *h:m* is replaced by the satellite image at (*h* + 1):00. Here, the predicted satellite image at (*h* + 1):00, is obtained from the Conv-LSTM model mentioned above.

Scheme 3: If *m* = 0, or 15, the satellite image at *h: m* is represented by the satellite image at *h:00*; if *m* = 45, the satellite image at *h:m* is represented by the satellite image at (*h* + 1):00. And if *m* = 30, then both satellite images at *h:00* and (*h* + 1):00 are used to predict the PV power, and the average power is used as the final forecasting result. Through the experimental analysis, this paper selects scheme 3 in the end.

Through the above-mentioned schemes, the cloud condition for every 15 min can be obtained. And then the concerned cloud region can be located according to the ACRS rule. Accordingly, the intra-hour cloud features can be extracted from the selected cloud region and utilized to predict the PV power with respect to the model mentioned below.

E. Modeling Process

In the modeling part, the PV power is predicted using the XGBoost algorithm, concerning the estimated cloud features and other factors. Fig. 8 shows the overall framework of the modeling process, including the training part and forecasting part.

The input information of the proposed approach is mainly divided into four parts. The first part is the pixel value of point *S*, which denotes the local cloud conditions. The second part is the mean value of concerned cloud region *R*, which denotes the regional cloud conditions. And the third part is historical power data, including lagged power values at time *T*-1, *T*-2, and *T*-3. Moreover, the temperature, humidity and solar zenith angle at time *T* constitute the fourth part, i.e., the other influencing factors.

For the training part, its main task is to adjust the parameters of the XGBoost. Firstly, the data, including the input information and the PV

Fig. 8. The framework of the modeling process.

power data for the latest two months are selected to construct the training datasets. Then, the XGBoost is trained with the training datasets to adjust the structure of trees and optimize the model parameters. Finally, the optimal model can be obtained after successive iterations. And in the forecasting part, the predicted power value can be obtained by inputting the related information into the trained model.

4. Case study

A. Data Source

The PV power data for every 15 min from Jul. 2017 to Dec. 2018 are collected from the PV station located in Ningxia, China. The satellite images with the pixel size of 1900*1300 are obtained from China Metrological Agency (CMA), which updates once per hour. All these data are used to demonstrate the effectiveness of the proposed approach. Since the solar radiation is almost zero at night, the data from 9 a.m. to 16 p.m. is chosen for the experiments. To ensure the universality of the model, the data from 1st to 20th for each month are utilized to train the model, and the rest data are utilized to test and analyze the forecasting results.

B. Evaluation Index

To evaluate the performance of the proposed models, three effective error measurement indices, i.e., the normalized mean absolute error (NMAE) [48], normalized root mean square error (NRMSE) [9] and the correlation coefficient (1-CORR) [21] are adopted in this paper, which can be respectively expressed as

$$NMAE = \frac{1}{N_{Total} \times P} \sum_{t=1}^{N_{Total}} |y(t)^* - y(t)|, \tag{19}$$

$$NRMSE = \frac{1}{P} \sqrt{\frac{1}{N_{Total}} \sum_{t=1}^{N_{Total}} (y(t)^* - y(t))^2}, \tag{20}$$

$$1 - CORR = 1 - \frac{Cov(Y^*, Y)}{\sqrt{Var(Y^*)}\sqrt{Var(Y)}}, \tag{21}$$

where $y(t)^*$ is the predicted PV power at time *t*, $y(t)$ is the actual PV power at time *t*, N_{Total} is the number of test samples, *P* is the installed capacity, *Y* and *Y** respectively represent the vector of the actual and predicted values of the test samples, *Cov* denotes the covariance, and *Var* denotes the variance.

C. Benchmarks

To verify the strength and potential of the proposed method in the PV power forecast, several models are selected as benchmarks for conducting the comprehensive study. Firstly, M1 is established to verify the effectiveness of the ACRS rule. M1 represents the forecasting model without region identification. Compared with the proposed method, M1 does not utilize the ACRS rule to recognize the concerned cloud region. Then, M2 and M3 are constructed to explore how model performance differs in the different input information. M2 only utilizes the cloud information obtained by the proposed method as input without considering the historical generation observations and metrological information. In contrast, M3 takes the historical generation observations and meteorological information as the input. Compared with the proposed method, M3 takes no account of the cloud information. In previous studies, the reliability and effectiveness of methods similar to M3 have been adequately tested. The M1, M2, M3 all utilize the XGBoost to achieve the PV power forecast, whose time resolution is set as 15 min. Moreover, all other forecasting conditions are identical.

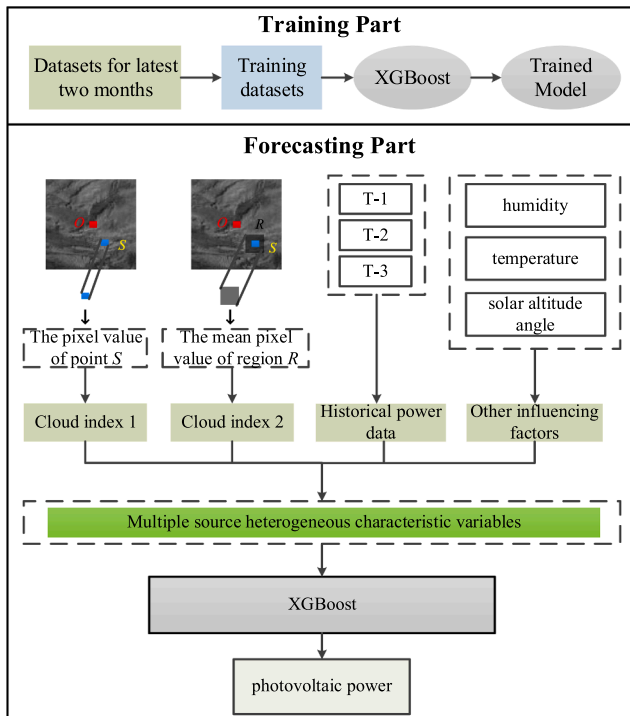Meanwhile, to illustrate the validity and effectiveness of the

proposed method, other benchmarks are selected for comparison. In solar forecasting tasks, the common practice is to select the persistence method (PM) [30] as the benchmark to verify the performance of other advanced approaches. PM takes the generation observation at time T-1 as the forecasting value at time T, which is helpful in the solar forecast. Therefore, the PM is chosen as an alternative benchmark in this paper.

LSTM shows excellent superiority in exploring the temporal correlation, which has been widely utilized for solar forecast [49]. Hence, the LSTM is selected as one of the benchmarks here.

More recently, the success in computer vision and deep learning have promoted the development of the CNN model. Some studies [20,22], relying on the CNN model to directly establish the mapping relationship between cloud images and PV power, have shown good performance. Therefore, in this paper, the CNN model is also included in the set of benchmarks.

D. Performance Analysis for the Proposed Method

Firstly, in this paper, the Conv-LSTM model is applied to the hourly satellite image forecast, which takes the nonlinear cloud motion into account. Fig. 9 shows the comparison between the predicted satellite images and the actual satellite images. Two kinds of loss functions are utilized for predicting the satellite image. One is the MSE, and the other is the SSIM. The test explores how model forecasting performance varies with the different loss functions. As shown in Fig. 8, the predicted image looks relatively fuzzy when MSE is used as a loss function. Theoretically, MSE measures the prediction accuracy according to the gap between the pixel matrices of two images. On the contrary, SSIM takes the brightness, contrast and structure of the image as the measure. Since SSIM can take more factors into account, the edges of the predicted image are clearer when using SSIM as the loss function. Meanwhile, it can also be seen from the figure that the Conv-LSTM model can take cloud thickness and shape changes into account and predict the nonlinear cloud movement. The predicted images are very similar to the actual images, which verifies the excellent performance of the Conv-LSTM model in solving spatial–temporal series prediction problems.

Then, M1 is selected as a comparison to verify the effectiveness of the ACRS rule. Fig. 10 shows the evaluation indexes of predicted values obtained by M1 and the method proposed in this paper, respectively. The error measurement indices NMAE, NRMSE, and 1-CORR, are applied to verify the effectiveness of the M1 and proposed method. And a smaller index indicates a more accurate forecasting result. It can be observed from the figure that the proposed method obtains better outcomes for all error measurement indices compared with M1. The NMAE
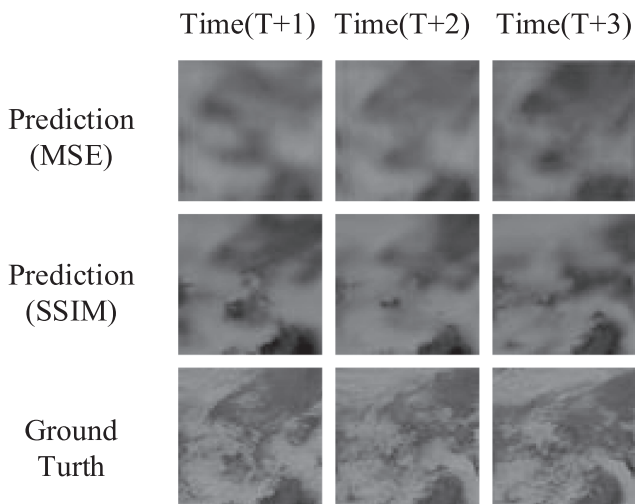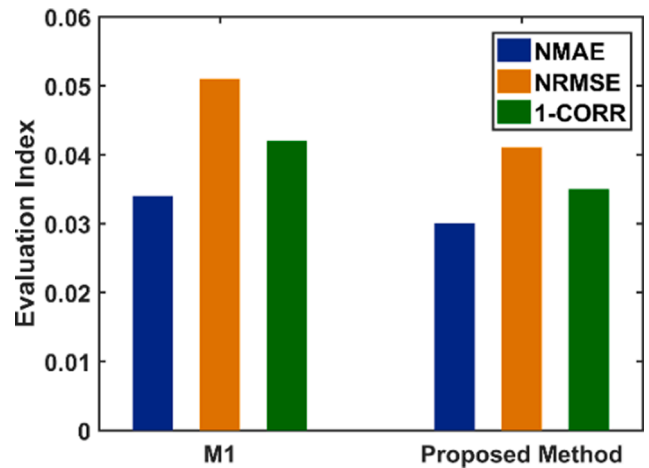

Fig. 10. The evaluation indexes of predicted PV power obtained by M1 and the proposed method, respectively.

and NRMSE values of the proposed method are about 8% lower than those of M1, while the 1-CORR of the proposed method is about 10% lower than that of M1. The results verify that a forecasting model with the ACRS rule can obtain a better forecasting performance.

Then, the three schemes of the SCRS algorithm are tested, respectively. Scatter plots of the actual results and forecasting results using scheme 1, scheme 2, and scheme 3 are displayed from left to right in Fig. 11. The scatter diagram reflects the degree of similarity between the predicted PV power values and the actual values. R^2 represents the coefficient of determination. The larger values of R^2 denote a higher precision. The scatter plots show that most of the pairs in scheme 1 are distributed around the $y = x$ line, but some pairs still have a significant error. And schemes 2 and 3 show a narrower band of distribution than scheme 1. Meanwhile, scheme 3 obtains a larger R^2 than scheme 2, which indicates scheme 3 is effective. Therefore, this paper selects scheme 3 as the scheme of the SCRS algorithm. In practice, the intra-hour cloud image is usually replaced with the cloud image on the previous hour, similar to scheme 1. However, scheme 2 and scheme 3 outperform scheme 1 in PV power forecast significantly in the tests. This also illustrates that the SCRS algorithm is valuable for improving prediction precision.

To verify the effectiveness of the proposed method, M2 and M3 are selected as the comparison. Fig. 12 and Fig. 13 show the PV power forecasting results from 9:00 am to 16:00 pm in cloudy conditions and sunny conditions, respectively.

As shown in Fig. 12, the forecasting results of the proposed method are much closer to the actual values than the results obtained by other benchmarks, indicating the effectiveness of the proposed method. There is an unavoidable delay in the forecasting results of the M3, which leads to the failure in reflecting the changes of the PV power in time. Compared with M3, the M2 shows a better performance, whose forecasting PV power curve is approximately the same as the actual one. This also illustrates that cloud occlusion information is more significant than
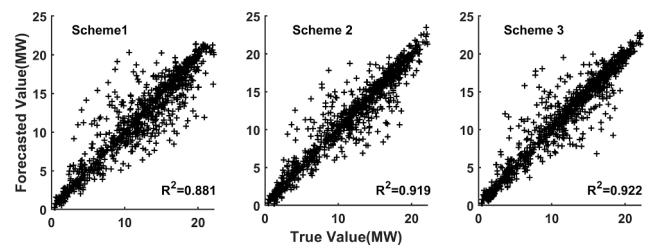

Fig. 9. The comparison of the predicted satellite image with the actual satellite image.

Fig. 11. The scatter plot of the actual results and forecasting results using scheme 1, scheme 2 and scheme 3, respectively.
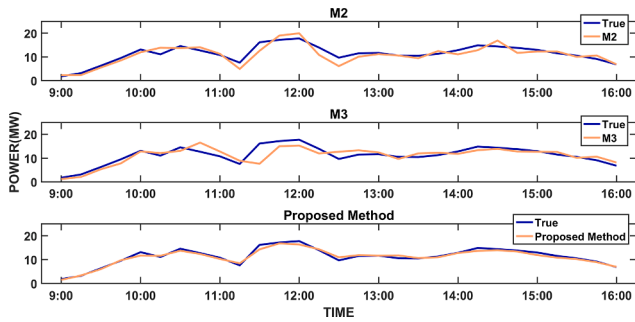
Fig. 12. The PV power forecasting results from 9:00 am to 16:00 pm in cloudy conditions.
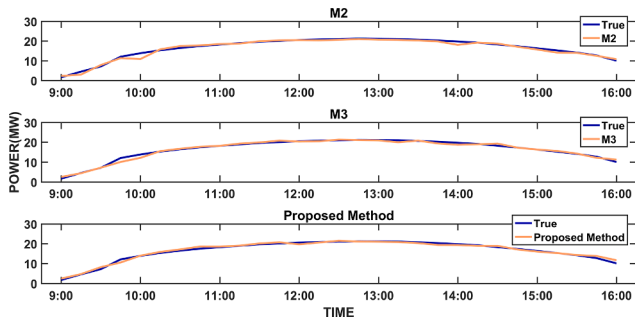

Fig. 13. The PV power forecasting results from 9:00 am to 16:00 pm in sunny conditions.

meteorological information for the ultra-short-term PV power forecast. Meanwhile, it is clear that meteorological information still plays an important role in improving the forecasting performance according to the fact that the proposed method outperforms M2. However, obtaining the numerical weather prediction data with high temporal and spatial resolution is pretty tricky. Therefore, satellite image-based forecasting methods play an indispensable role in PV power forecast. On the contrary, there are few clouds in sunny conditions, making it difficult for satellite images to provide additional useful information. Therefore, the forecasting results of the method mentioned above are very similar and both close to the actual value, as illustrated in Fig. 13.

All benchmark models are evaluated, and the quantitative results are summarized in Table 1. Since the performance of M3 has been fully verified in previous studies, M3 is selected as the baseline to measure the performance of other models. As shown in Table 1, the other models all outperform M3 except for PM. Compared with M3, the forecasting performance of M1 and M2 improves to a certain extent, verifying that the cloud information extracted from satellite images has obvious effects on strengthening the forecasting performance. Meanwhile, the NMAE value of the proposed method is about 16% lower than M3, while the NRMSE value is 21% lower. This also illustrates the effectiveness of the proposed method. Moreover, the LSTM and CNN model performs approximately as well as XGBoost model used in this paper. However,

these two models, especially CNN, will spend more time on training and forecasting due to the model complexity. Since the main advantage of the XGBoost is its fast computing speed, the training speed of the proposed method is much faster. For ultra-short-term PV power forecast, the accuracy and rapidity of the model are both significant. Therefore, the method proposed in this article achieves the best performance from a comprehensive perspective.

Moreover, to verify the forecasting performance of the model at different time scales, the proposed method, M1 and M3, are tested for the forecasting horizon of 15 min, 30 min, and 60 min, respectively. Table 2 shows the evaluation indexes corresponding to the three models. It can be seen from the table that the proposed method gains the smallest NMAE and NRMSE values for all horizons, which indicates that its performance is the best. The NMAE values of M1 are about 13% higher than the values for the proposed method in 15-min and 30-min ahead forecasting and are 14% higher in the 60-min forecasting horizon. In addition, the NRMSE values of M1 are about 10%, 17%, and 14% higher than the values for the proposed method in15-min, 30-min, and 60-min, respectively. This phenomenon is due to that more relevant cloud features are extracted using the ACRS rule. The relevant cloud features can reflect the shielding effects of clouds on irradiance and the fluctuation of PV power, which is crucial to improve the forecasting precision. Meanwhile, the proposed method outperforms M3 for all the horizons, confirming the effectiveness of including cloud information for PV power forecast.

5. Conclusions

In this paper, a novel satellite image-based approach for photovoltaic power forecast is proposed. The hourly satellite image variation is predicted using Conv-LSTM, which takes the nonlinear cloud motion into account, providing more accurate cloud movement trajectories. The active cloud region selection rule is derived based on the changing solar location to dynamically select the concerned cloud region in the satellite image. Thus, it can precisely quantify the cloud shielding effects that cause the fluctuations of PV power. Accordingly, the SCRS algorithm is developed to estimate the intra-hour variation of the cloud. Based on the ACRS rule and the SCRS algorithm, the cloud features can be extracted at any predetermined time step from the low-frequency satellite images. Therefore, the model can meet the requirement of ultra-short-term power prediction and improve the practicability of satellite images in photovoltaic power forecast. The outstanding performance illustrates that the proposed approach is effective in achieving ultra-short-term PV power forecast based on the low update frequency satellite images. The method proposed in this paper is mainly applied to the photovoltaic power station with a relatively broad spatial scope. Meanwhile, the framework of the proposed method can also be applied to different scenarios, such as solar panels on the roof or in the fields. For these scenarios with a small spatial scope, it should choose the satellite images with the high spatial resolution for photovoltaic power forecast.

Table 1
The quantitative results and relative improvement of all benchmarks.

NO	Model	Metrics		Relative Improvement(%)	
		NMAE	NRMSE	NMAE	NRMSE
1	Proposed Method	0.030	0.041	16.66	21.15
2	PM	0.062	0.089	−72.22	−71.15
3	M1	0.034	0.051	5.55	1.92
4	M2	0.035	0.047	2.77	9.61
5	M3	0.036	0.052	0	0
6	LSTM	0.033	0.044	8.33	15.38
7	CNN	0.031	0.041	13.88	21.15

Table 2
The evaluation indexes for the horizon of 15 min, 30 min, and 60 min.

Method	Horizon	NMAE	NRMSE
Proposed Method	15 min	0.030	0.042
	30 min	0.032	0.046
	60 min	0.035	0.049
M1	15 min	0.034	0.046
	30 min	0.036	0.054
	60 min	0.040	0.056
M3	15 min	0.036	0.048
	30 min	0.038	0.053
	60 min	0.041	0.058

CRediT authorship contribution statement

Zhiyuan Si: Writing - original draft. **Ming Yang:** Supervision, Validation, Writing - review & editing. **Yixiao Yu:** Project administration. **Tingting Ding:** Data curation.

Declaration of Competing Interest

The authors declare that they have no known competing financial interests or personal relationships that could have appeared to influence the work reported in this paper.

References

[1] Kabir E, Kumar P, Kumar S, Adelodun A, Kim K. Solar energy: Potential and future prospects. Renew Sustain Energy Rev 2018;82:894–900.

[2] Wang Z, Wang F, Su S. Solar Irradiance Short-Term Prediction Model Based on BP Neural Network. Energy Procedia 2011;12:488–94.

[3] Shah R, Mithulananthan N, Bansal RC, Ramachandara-murthy VK. A review of key power system stability challenges for largescale PV integration. Renew Sustain Energy Rev 2015;41:1423–36.

[4] Nanou SI, Papakonstantinou AG, Papathanassiou SA. A generic model of two-stage grid-connected PV systems with primary frequency response and inertia emulation. Electr Power Syst Res 2015;127:186–96.

[5] F. Wang, Z. Zhen, Z. Mi, H. Sun, S. Su, and G. Yang, "Solar irradiance feature extraction and support vector machines based weather status pattern recognition model for short-term photovoltaic power forecasting," Energy and buildings, vol. 86, pp. 427–438, Jan. 2015.

[6] F. Wang, H. Xu, T. Xu, K. Li, M. Shafie-khah, and J. P. S. Catalão, "The values of market-based demand response on improving power system reliability under extreme circumstances," Applied Energy, vol. 93, pp. 220–231, Mar. 2017.

[7] De Giorgi MG, Congedo PM, Malvoni M. Photovoltaic power forecasting using statistical methods: impact of weather data. IET Sci Meas Technol 2014;8:90–7.

[8] Yang HT, Huang CM, Huang YC, Pai YS. A weather-based hybrid method for 1-day ahead hourly forecasting of PV power output. IEEE Trans Sustain Energy 2014;5 (3):917–26.

[9] Theocharides S, Makrides G, Livera A, Theristis M, Kaimakis P, Georghiou G. Day-ahead photovoltaic power production forecasting methodology based on machine learning and statistical post-processing. Appl Energy 2020;268:115023.

[10] Mathiesen P, Kleissl J. Evaluation of numerical weather prediction for intra-day solar forecasting in the continental United States. Sol Energy 2011;85(5):967–77.

[11] Lorenz E, Hurka J, Heinemann D, Beyer HG. Irradiance forecasting for the power prediction of grid-connected photovoltaic systems. IEEE J Sel Top Appl Earth Obs Remote Sens 2009;2:2–10.

[12] Caldas M, Alonso-Suárez R. Very short-term solar irradiance forecast using all-sky imaging and real-time irradiance measurements. Renew Energy 2019;143:1643–58.

[13] Du J, Min Q, Zhang P, Guo J, Yang J, Yin B. Short-Term Solar Irradiance Forecasts Using Sky Images and Radiative Transfer Model. Energies 2018;11(5):1107.

[14] Yang H, Kurtz B, Nguyen D, Urquhart B, Chow C, Ghonima M, et al. Solar irradiance forecasting using a ground-based sky imager developed at UC San Diego. Sol Energy 2014;133:502–24.

[15] Yang J, Min Q, Lu W, Yao W, Ma Y, Du J, et al. An automated cloud detection method based on the green channel of total-sky visible images. Atmos Meas Tech 2015;8:4671–9.

[16] Liu L, Sun X, Chen F, Zhao S, Gao T. Cloud Classification Based on Structure Features of Infrared Images. J Atmos Oceanic Technol 2011;28:410–7.

[17] Huo J, Lu D. Cloud Determination of All-Sky Images under Low-Visibility Conditions. J Atmos Oceanic Technol 2009;26:2172–81.

[18] Peng Z, Yu D, Huang D, Heiser J, Yoo S, Kalb P. 3D cloud detection and tracking system for solar forecast using multiple sky imagers. Sol Energy 2015;118:496–519.

[19] Sun Y, Wang F, Zhen Z, Mi Z, Liu C, Wang B, et al. Research on short-term module temperature prediction model based on BP neural network for photovoltaic power forecasting. In: 2015 IEEE Power Energy Soc. Gen. Meeting; 2015. p. 1–5.

[20] Sun Y, Szucs G, Brandt AR. Solar PV output prediction from video streams using convolutional neural networks. Energy Environ Sci 2018;11(7):1811–8.

[21] Zhen Z, Liu J, Zhang Z, Wang F, Chai H, Yu Y, et al. Deep Learning Based Surface Irradiance Mapping Model for Solar PV Power Forecasting Using Sky Image. IEEE Trans Industry Appl 2020;56(4):3385–96.

[22] Kong W, Jia Y, Dong Z, Meng K, Chai S. Hybrid approaches based on deep whole-sky-image learning to photovoltaic generation forecasting. Appl Energy 2020;280.

[23] Wan C, Zhao J, Song Y, Xu Z, Lin J, Hu Z. Photovoltaic and solar power forecasting for smart grid energy management. CSEE J Power Energy Syst 2015;1:38–46.

[24] Scheck L, Weissmann M, Mayer B. Efficient Methods to Account for Cloud-Top Inclination and Cloud Overlap in Synthetic Visible Satellite Images. J Atmos Oceanic Technol 2018;35:665–85.

[25] Nunes A, Marçal A, Vaughan R. Fast over-land atmospheric correction of visible and near-infrared satellite images. Int J Remote Sens 2008;29:3523–31.

[26] Geraldi E, Romano F, Ricciardelli E. An advanced model for the estimation of the surface solar irradiance under all atmospheric conditions using MSG/SEVIRI data. IEEE Trans Geosci Remote Sens 2012;50(8):2934–53.

[27] Rodríguez-Benítez F, López-Cuesta M, Arbizu-Barrena C, Fernández-León M, Pamos-Ureña M, Tovar-Pescador J, et al. Assessment of new solar radiation nowcasting methods based on sky-camera and satellite imagery. Appl Energy 2021;292:116838.

[28] Aguiar LM, Pereira B, Lauret P, Díaz F, David M. Combining solar irradiance measurements, satellite-derived data and a numerical weather prediction model to improve intra-day solar forecasting. Renew Energy 2016;97:599–610.

[29] A. Hammer, D. Heinemann, E. Lorenz, C. Hoyer, and B. Lückeke, "Short-term forecasting of solar radiation: a statistical approach using satellite data," Solar Energy, vol. 67, pp. 139–150, 1999.

[30] Marquez R, Pedro HT, Coimbra CF. Hybrid solar forecasting method uses satellite imaging and ground telemetry as inputs to ANNs. Sol Energy 2013;92:176–88.

[31] Kato T, Manabe Y, Funabashi T, Yoshiura T, Kurimoto M, Suzuoki Y. A Study on Several Hours Ahead Forecasting of Spatial Average Irradiance using NWP model and Satellite Infrared Image. In: 2016 International Conference on Probabilistic Methods Applied to Power Systems (PMAPS); 2016. p. 1–8.

[32] Magnone L, Sossan F, Scolari E, Paolone M. Cloud Motion Identification Algorithms Based on All-Sky Images to Support Solar Irradiance Forecast. In: 2017 IEEE 44th Photovoltaic Specialist Conference (PVSC); 2017. p. 1415–20.

[33] Quesada-Ruiz S, Chu Y, Tovar-Pescador J, Pedro HTC, Coimbra CFM. Cloud-tracking methodology for intra-hour DNI forecasting. Sol Energy 2014;102:267–75.

[34] Sirch T, Bugliaro L, Zinner T, Möhrlein M, Vazquez-Navarro M. Cloud and DNI nowcasting with MSG/SEVIRI for the optimized operation of concentrating solar power plants. Atmos Meas Tech 2017;10(2):409–29.

[35] W. Richardson, H. Krishnaswam, R. Vega, M. Cervantes, "A low cost, edge computing all-sky imager for cloud tracking and intra-hour irradiance forecasting," Sustainability, vol. 9, 2017.

[36] Shi X, Chen Z, Wang H, Yeung D, Wong W, Woo W. Convolutional LSTM network: A machine learning approach for precipitation nowcasting. Adv Neural Info Process Syst 2015:802–10.

[37] Zhu X, Wu J, Zhou H, Ding J, Cui F, Zhao X. Very short-term prediction model for photovoltaic power based on improving the total sky cloud image recognition. J Eng 2017:1947–52.

[38] Tang J, Lv Z, Zhang Y, Yu M, Wei W. An improved cloud recognition and classification method for photovoltaic power prediction based on total-sky-images. J Eng 2019:4922–6.

[39] R. Perez, S. Kivalov, J. Schlemmer, K. Hemker Jr, D. Renńe, and T. E. Hoff, "Validation of short and medium term operational solar radiation forecasts in the US," Solar Energy, vol. 84, no. 12, pp. 2161–2172, 2010.

[40] Dong Z, Yang D, Reindl T, Walsh W. Satellite image analysis and a hybrid ESSS/ANN model to forecast solar irradiance in the tropics. Energy Convers Manage 2014;79:66–73.

[41] Wang Z, Hong T, Piette M. Building thermal load prediction through shallow machine learning and deep learning. Appl Energy 2020;263:114683.

[42] Lopes AT, Aguiar E, De S, Alberto F, Oliveira-Santos T. Facial expression recognition with Convolutional Neural Networks: Coping with few data and the training sample order. Pattern Recogn 2017;61:610–28.

[43] Zhang J, Yan J, Infield D, Liu Y, Lien F. Short-term forecasting and uncertainty analysis of wind turbine power based on long short-term memory network and Gaussian mixture model. Appl Energy 2019;241:229–44.

[44] Niu D, Diao L, Xu L, Zhang Z, Chen X, Liang S. Precipitation forecast based on multi-channel ConvLSTM and 3D-CNN. In: 2020 International Conference on Unmanned Aircraft Systems; 2020. p. 361–71.

[45] H. Zheng and Y. Wu, "A XGBoost Model with Weather Similarity Analysis and Feature Engineering for Short-Term Wind Power Forecasting," Applied Sciences, vol. 9, no. 15, 2019.

[46] Cai R, Xie X, Wang B, Yang R, Xu D, He Y. Wind Speed Forecasting Based on Extreme Gradient Boosting. IEEE Access 2020;8:175063–9.

[47] Si Z, Yu Y, Yang M, Li P. Hybrid Solar Forecasting Method Using Satellite Visible Images and Modified Convolutional Neural Networks. IEEE Trans Industry Appl 2021;57(1):5–16.

[48] Sun M, Feng C, Zhang J. Conditional aggregated probabilistic wind power forecasting based on spatio-temporal correlation. Appl Energy 2019;256:113842.

[49] Srivastava S, Lessmann S. A comparative study of LSTM neural networks in forecasting day-ahead global horizontal irradiance with satellite data. Sol Energy 2018;162:232–47.